Ru Loaded Biphasic TiO2 Nanosheet-Tubes Enriched with Ti3+ Defects and Directionally Deficient Electrons as Highly Efficient Catalysts in Benzene Selective Hydrogenation

Shuo Wang , Xianrui Chen , Shuangsheng Xiong , Xiaoting Zhang , Li Hou * , Qian Zhang , Yatao Wang , Faming Gao *

Posted Date: 12 December 2023

doi: 10.20944/preprints202312.0881.v1

Keywords: TiO2 nanosheet tubes; crystalline phases; Ti3+ defects; electron-deficient Ru; benzene selective hydrogenation

Article

Ru Loaded Biphasic TiO_2 Nanosheet-Tubes Enriched with Ti^{3+} Defects and Directionally Deficient Electrons as Highly Efficient Catalysts in Benzene Selective Hydrogenation

Shuo Wang [1], Xianrui Chen [1], Shuangsheng Xiong [1], Xiaoting Zhang [1], Li Hou [1,*], Qian Zhang [2], Yatao Wang [2] and Faming Gao [1,3,*]

[1] Key Laboratory of Applied Chemistry, Yanshan University, Qinhuangdao 066004, China
[2] Kailuan Energy and Chemical Co., Ltd., Tangshan 063018, China
[3] College of Chemical Engineering and Materials Science, Tianjin University of Science and Technology, Tianjin 300457, China
* Correspondence: holy@ysu.edu.cn (L.H.); fmgao@ysu.edu.cn (F.G.)

Abstract: Crystalline phase engineering is a prominent strategy for synergistically optimizing the surface-body phases of a catalyst. In this work, TiO_2 nanosheets assembled into nanotubes (TNSTs) with two-phases of anatase and rutile were firstly synthesized via crystal engineering by simple thermal annealing, and subsequently loaded with Ru nanoparticles to create efficient benzene hydrogenation catalyst Ru/TNSTs. The well- designed nanosheet-tubes structure boasts large specific surface area and excellent transmission channels, which effectively prevents the agglomeration and deactivation of loaded Ru nanoparticles, as well as promotes the internal diffusion in the reaction process of benzene hydrogenation to cyclohexene. Furthermore, titanium dioxide nanosheet-tubes contain numerous Ti^{3+} defects, which not only improves the overall generation rate of cyclohexene, but also enhances the suppression of cyclohexene adsorption. Most importantly, the two-phases of titanium dioxide increases the ratio of the electron deficiencies of Ru and promotes cyclohexene desorption. These synergistic properties enhance the selectivity and efficiency of the Ru/TNSTs catalysts, resulting in excellent performance in the hydrogenation of benzene to cyclohexene. Especially the Ru/TNSTs-4 catalyst achieves a 95% initial selectivity and 51% yield of cyclohexene in the reaction, outperforming most supported Ru-based catalysts. This work may provide new perspectives for designing efficient benzene hydrogenation catalysts via crystalline phase engineering.

Keywords: TiO_2 nanosheet tubes; Crystalline phases; Ti^{3+} defects; Electron-deficient Ru; Benzene selective hydrogenation

1. Introduction

Cyclohexene, featuring an active carbon-carbon double bond, is a crucial chemical intermediate. It can readily be adducted for the production of high-value industrial raw materials like nylon, cyclohexanone, and caprolactam through traditional olefinic reactions [1–3]. Selective hydrogenation of benzene to prepare cyclohexene is a common route for industrial synthesis, unfortunately, the standard Gibbs free energy change for the selective hydrogenation of benzene to produce cyclohexane is thermodynamically lower($\Delta_r G_m^\theta$ == -98 kJ mol^{-1}) than that for the production of cyclohexene ($\Delta_r G_m^\theta$ = -23 kJ mol^{-1}) [4,5]. This suggests that the selective conversion of benzene to cyclohexane is thermodynamically preferred, making it an easier process, while the production of cyclohexene is comparatively more difficult. Therefore, in order to enhance the cyclohexene yield from benzene selective hydrogenation, the development of appropriate catalysts is indeed required. Such catalysts should be capable of modulating the relative rates of the two-step hydrogenation reactions, i.e., benzene to cyclohexene and cyclohexene to cyclohexane [6–8], thereby yielding more cyclohexene product. Currently, non-loaded RuZn catalysts are widely used in industry [9,10], but they have drawbacks, including a high amount of precious metal Ru and poor catalyst stability.

 doi:10.20944/preprints202312.0881.v1

Additionally, the zirconia additive, used to prevent the agglomeration of RuZn, is challenging to control the dispersion. Thus, there is an urgent need to develop low-cost, high-activity catalysts and engineer their surface properties for improved cyclohexene selectivity.

Supported catalysts have been widely used in non-homogeneous reactions due to their advantages such as high dispersion, low dosage of active components, and high catalyst-substrate contact efficiency, as well as good economic and environmental characteristics. Among the many commonly used carriers for loaded catalysts, oxide carriers have been widely used because of their chemical stability, thermal stability, and modulation properties of acid-base properties, such as TiO_2 [11,12], SiO_2 [13,14], Al_2O_3 [15], CeO_2 [16], and ZrO_2 [17]. Among these, the strong interaction between titanium dioxide carriers and metals can effectively regulate the dispersion of active metals [18–20]. This optimizes the adsorption of reactants on the catalyst surface, resulting in a catalyst with excellent activity and thermal stability, making TiO_2 widely used in benzene hydrogenation reactions.

To date, a number of methods for engineering titanium dioxide to improve cyclohexene selectivity in benzene hydrogenation reactions have been developed, which provide valuable insights into how to optimize the performance of catalysts by tuning the properties of TiO_2, such as surface species tuning [21,22], polycrystalline structure manipulation [23,24], crystalline surface control [8,25], and morphology manipulation [26], etc. Among these, the design of titanium dioxide morphology and the modulation of crystal properties are deemed the most practical and effective approaches to enhancing catalyst performance. For example, constructing titanium dioxide into nanoflower spheres [8], nanosheets [27], and various other forms has been shown significantly enhance the activity in selective hydrogenation reaction of benzene. In a recent study, Zhou and colleagues have found that the initial selectivity of catalysts for benzene to cyclohexene hydrogenation can be notably enhanced by adjusting the anatase to rutile TiO_2 molar ratio using crystalline phase engineering techniques [23]. However, the synergistic effect of the carrier structure and the phases on the benzene hydrogenation performance remains to be explored.

In this work, unique structures with TiO_2 nanosheets assembled nanotubes (TNSTs) were prepared using a solvothermal method, where the ratio of specific crystalline phases was modulated by a simple adjustment of the annealing time, and the effect of synergism between the two on the properties of benzene selective hydrogenation was investigated. The distinctiveness of this structure lies in the numerous intersecting nanosheets on the tubes, which effectively prevents the agglomeration and deactivation of supported Ru microcrystals caused by the collision of Ru particles, thus enhancing the stability of the catalysts. Furthermore, the specific crystalline phases increase the proportion of electron-deficient Ru. The Ti^{3+} deficiency introduced by the crystal phase modulation promotes the desorption of cyclohexene and also inhibits the absorption of cyclohexene. This dual action effectively enhances the net rate of cyclohexene generation. The integrating of nanostructures and defects of Ru/TNSTs catalysts notably amplifies the productivity of cyclohexene in the selective hydrogenation of benzene. This investigation may offer fresh insights into the creation of effective catalysts for non-homogeneous hydrogenation processes.

2. Results and Discussion

Figure 1a depicts the systematic process of the preparation of Ru/TNSTs catalysts. The procedure initiated with the synthesis of a precursor using a simple solvothermal method. Firstly, titanium oxy sulfate was dispersed in ethanol and formed a uniform solution. During this process, the titanium oxy sulfate molecules started to undergo progressive hydrolysis. The subsequent addition of glycerol and diethyl ether solvent further stabilized the reaction system, and glycerol could form a stable complex with titanium ions in titanium oxy sulfate. This interaction effectively prevented premature polymerization, thereby lending further stability to the reaction system. As the hydrolysis of the titanium oxy sulfate persisted, a condensation reaction ensued, giving birth to a Ti-O-Ti skeletal structure. Simultaneously, the complex formed by titanium ions and glycerol began to dissociate gradually, releasing titanium ions to participate in the condensation reaction. This led to the genesis of a larger Ti-O-Ti skeleton under hydrothermal conditions, which gradually rearranged into a nanotube-like structure. Following this, the pure nanotube precursor underwent high-temperature

Preprints (www.preprints.org) | NOT PEER-REVIEWED | Posted: 12 December 2023 doi:10.20944/preprints202312.0881.v1

calcination, ensuring the complete evaporation of moisture and organic matter. The end product was a nanotube carrier that exhibited a unique nanosheet assembly morphology. By fine-tuning the high-temperature annealing duration, the crystalline phase and structure of the TiO_2 carrier could be adjusted. The final step involved the integration of the active metal ruthenium through the incorporation chemical reduction method to create the desired Ru/TNSTs-t (t= annealing time of 2, 4, and 6 hours) catalysts.

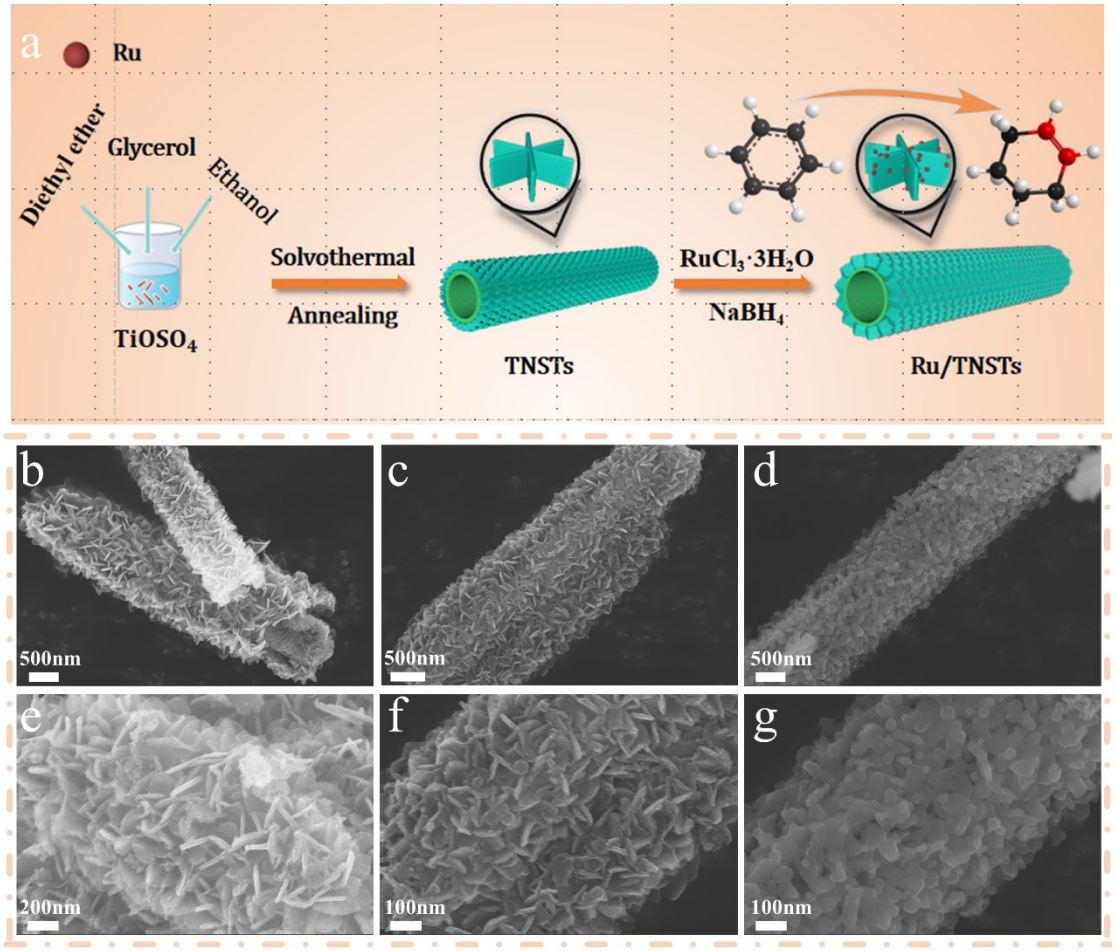

Figure 1. Schematic diagram of the synthesis process of Ru/TNSTs catalyst (a); SEM images of Ru/TNSTs-2 (b, e), Ru/TNSTs-4 (c, f), and Ru/TNSTs-6 (d, g) catalysts.

The morphology of the synthesized TNSTs-t carrier and the Ru/TNSTs-t catalysts was analyzed using scanning electron microscopy (SEM) as shown in Figure S1 and Figure 1b-g. It can be observed that the materials' morphology remains largely unchanged before and after loading. All Ru/TNSTs-t catalyst samples show nanotube structures. Specifically, the surfaces of Ru/TNSTs-2 and Ru/TNSTs-4 catalyst nanotubes feature a tightly arranged overlay of crisscrossing nanosheets. These 2D nanosheets were assembled into tubular structures, thus avoiding disordered distribution and overlapping of nanosheets. This architecture guarantees a uniform distribution of the active metal Ru on the nanosheets. It aids in protecting the Ru microcrystals from deactivation caused by the collision of loaded Ru nanoparticles throughout the reaction process, thereby enhancing the catalyst's stability. It is noteworthy that when the annealing process extended to 6 h, the uniform nanoparticles instead of nanosheets have appeared on the nanotube surface of the Ru/TNSTs-6 catalysts, as shown in Figure 1g. This may be due to the fact that the crystalline morphology of titanium dioxide changes from anatase to a more stable rutile type as the annealing time increases. During this process, collapse and aggregation of nanosheets has occurred.

 doi:10.20944/preprints202312.0881.v1

To thoroughly examine the microstructure of the catalysts, the transmission electron microscopy (TEM) technique was utilized to precisely characterize the synthesized Ru/TNSTs-t. Figure S2 exhibits the detailed tubular configurations of the Ru/TNSTs-2 and Ru/TNSTs-6 catalysts, which correspond closely with the SEM-derived observations. In particular, representative Ru/TNSTs-4 sample exhibits well-designed nanosheet-tubes structure, as shown in Figure 2a, b. As revealed in Figure 2c, ruthenium nanoparticles are uniformly dispersed across the nanosheets, indicating the successful synthesis of the Ru/TNSTs material. Figure 2d presents an image captured by high-resolution transmission electron microscopy (HRTEM) of Ru/TNSTs-4, revealing the crystalline lattice structure of the material. A clear lattice spacing of 0.21 nm aligns with the (101) crystalline plane of ruthenium could be found. This finding indicates that the deposited ruthenium nanoparticles (Ru NPs marked by yellow circles) are of a crystalline nature. Moreover, HRTEM in Figure 2d shows lattice spacings of 0.32 nm and 0.35 nm, which could be attributed to the (110) crystal plane of rutile titanium dioxide and the (101) crystal plane of anatase titanium dioxide, respectively. Meanwhile, the (111) crystal plane of rutile was also observed as shown in Figure 2e, from which it can be seen that there are many adjacent interfaces between the rutile and anatase phases (indicated by blue dashed lines) and that many crystalline rutheniums have been deposited at the junctions. Detailed observation of the crystalline phase junctions in Figure 2d reveals numerous dislocations and distortions (marked by red circles), suggesting the formation of a defect-rich Ru/TNSTs-4 structure. The STEM-EDS elemental mapping (Figure 2f-i) confirms the existence of elements O, Ti, and Ru, along with their relatively uniform distribution throughout the nanotube structure, affirming the excellent dispersion of ruthenium.

Preprints (www.preprints.org) | NOT PEER-REVIEWED | Posted: 12 December 2023 doi:10.20944/preprints202312.0881.v1

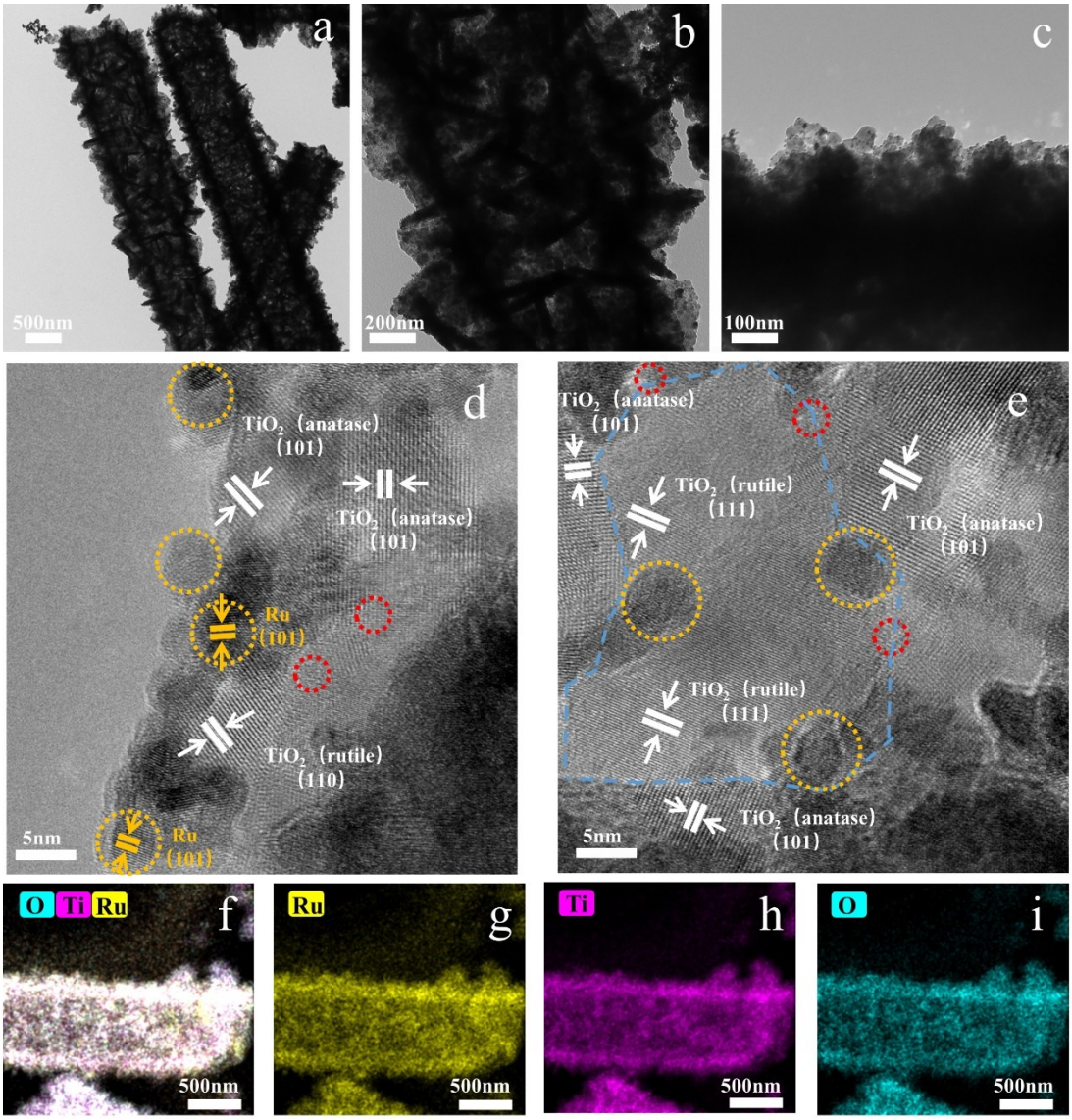

Figure 2. (a, b, c) TEM images of Ru/TNSTs-4; (d, e) HRTEM images of the rectangular area; and (f-i) EDX spectra of the as-synthesized Ru/TNSTs-4 catalyst.

The crystalline phase evolution of the nanotube carriers was further explored by X-ray diffraction (XRD) as shown in Figure 3A and Figure S3. Comparison reveals that the crystalline phase and crystallinity of the samples before and after loading do not change significantly. Further analysis of Figure 3A reveals that the crystal structure of the prepared TiO_2 carrier changes significantly with the adjustment of annealing time. The Ru/TNSTs-4 sample exhibits an optimal balance between the anatase phase (JCPDS 21-1272) and rutile phase (JCPDS 21-1276), where the anatase phase prevails as the primary phase in the Ru/TNSTs-2 sample with reduced annealing duration. On the contrary, with prolonged annealing time, the anatase phase significantly diminishes, while the rutile phase emerges as the predominant phase in the Ru/TNSTs-6 sample. This implies that the phase begins to shift from anatase to rutile as the annealing time increases, suggesting that the ratio of crystalline phases in the catalyst carrier could be adjusted by changing the annealing time. These results are in agreement with the morphology evolution, further revealing the formation process of the material. To confirm the presence of Ru, fine XRD investigation was carried out, as shown in Figure S4. It could be found that even with a theoretical incorporation of ruthenium reaching 10 wt%, the anticipated prominent diffraction peak of ruthenium (Ru) (101) at 44.0° is not discernible. This may be attributed to the small ruthenium particle sizes and high degree of dispersion [28]. Nitrogen adsorption-desorption assays were conducted to assess the catalyst samples' surface area and pore size

Preprints (www.preprints.org) | NOT PEER-REVIEWED | Posted: 12 December 2023 doi:10.20944/preprints202312.0881.v1

distribution. As Figure 3B demonstrates, all samples show characteristic type IV isotherms and H3 hysteresis loops, indicative of mesoporous structures [29]. Observations indicate a relatively uniform pore size distribution in the samples (Figure 3C), particularly for Ru/TNSTs-4, which demonstrates a complex pore structure combining microporous and mesoporous characteristics. The BET surface areas of the samples are relatively consistent, varying from 20 to 39 m^2/g (Table S1). Among these samples, the Ru/TNSTs-4 sample boasts the largest specific surface area and an optimal pore size; this structure facilitates enhanced diffusion of reactants and products, potentially leading to improved catalytic efficiency in reactions.

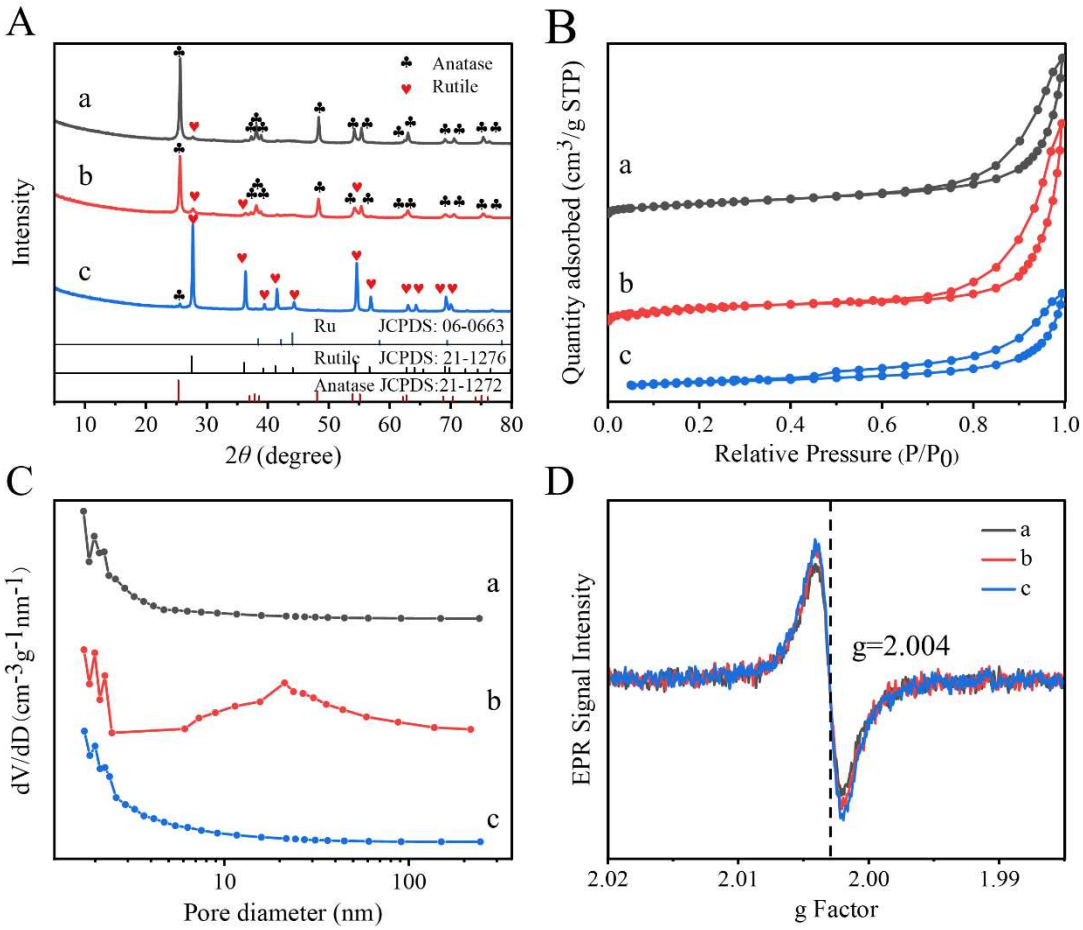

Figure 3. X-ray Diffraction Patterns (A), Nitrogen Adsorption-Desorption Isotherms (B), Pore Size Distribution (C), and Electron Paramagnetic Resonance Spectra (D) for Ru/TNSTs-2 (a), Ru/TNSTs-4 (b), and Ru/TNSTs-6 (c) catalysts.

Given the high sensitivity of electron paramagnetic resonance (EPR) for identifying paramagnetic centers with unpaired electrons, this technique was utilized to investigate the occurrence of oxygen vacancy (O_V) and Ti^{3+} defects in the Ru/TNSTs-t catalysts. As illustrated in Figure 3D, no conspicuous EPR signals are identified in the range of g= 1.94-1.99 for Ti^{3+} [30]. Nonetheless, a pronounced signal peak is discernible at g = 2.004, this peak stems from the oxygen-negative (O^-) species generated by the adsorption of Ti^{3+} on the surface to dissociate the O_2 in the air, thereby corroborating the existence of Ti^{3+} and oxygen vacancies in all three materials [27,31,32]. Since there is a proportional relationship between signal intensity and Ti^{3+} defect content [33], and the Ru/TNSTs-4 and Ru/TNSTs-6 catalysts have more Ti^{3+} defect content, it is reasonable to propose that the duration of annealing plays a role in the formation of Ti^{3+} defects.

To probe deeper into the chemical state and Ti^{3+} deficiency in the synthesized Ru/TNSTs-t catalysts, X-ray photoelectron spectroscopy (XPS) analysis was conducted. Figure 4A shows the full spectrum of Ru/TNSTs-t. Signals of Ru, Ti, elemental O, and trace contaminant C can be seen, but there is no signal of Cl-, which suggests that Cl- has been completely removed during the preparation

Preprints (www.preprints.org) | NOT PEER-REVIEWED | Posted: 12 December 2023 doi:10.20944/preprints202312.0881.v1

process. Figure 4B shows the three-dimensional spectrum of Ru with peaks in the ranges of 280.3 ~ 280.5 eV and 281.9 ~ 282.1 eV attributed to the electron-deficient $Ru^{\delta+}$ in metal Ru0 and Ru 3d5/2 [34,35]. Table S2 summarizes the corresponding binding energies (BE) in the Ru 3d5/2 region of the catalyst, indicating that the Ru NPs are in the metallic state with a certain amount of electron-deficient $Ru^{\delta+}$ [36], which originated from the Ru-O linkages connecting the Ru NPs with the rutile/anatase junction [24]. Figure 4C presents the Ti 2p spectra for the Ru/TNSTs-t catalysts, predominantly featuring two components. The low-energy Ti 2p3/2 peaks are discerned at BE of 458.8 eV and 457.3 eV, corresponding to the oxidation states of Ti^{4+} and Ti^{3+} [34,37]. Titanium mainly exists in the Ti^{4+} state, while the detection of a Ti^{3+} state aligns with the observations reported in EPR studies. Figure 4D exhibits the O 1s XPS spectra of the catalysts, and peaks near 530.0, 531.8, and 533.5 eV are attributed to lattice oxygen (O_L), oxygen vacancies (O_V), and adsorbed water (H_2O) [21,34,38]. In conclusion, both EPR and XPS indicate the presence of a small amount of electron-deficient $Ru^{\delta+}$, as well as partially Ti^{3+} and O_V on the Ru/TNSTs-t catalyst. In addition, when the annealing time of TNSTs-t extends from 2 to 6 hours, the defect content changes to some extent, indicating that the calcination time affects the defect content to some extent by influencing the crystalline phase changes.

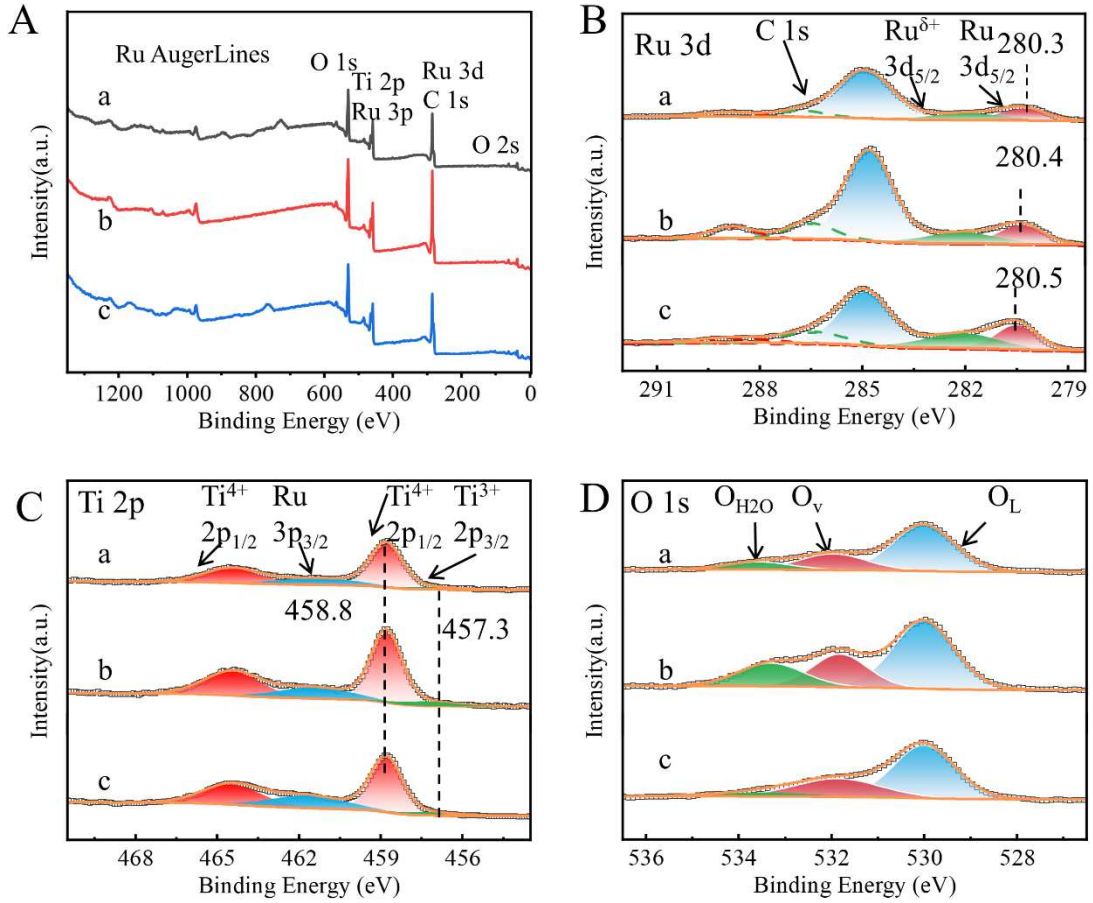

Figure 4. Full XPS spectra (A), Ru 3d XPS spectra (B), Ti 2p XPS spectra (C), and O 1s core-level spectra (D) of the as-synthesized Ru/TNSTs-2 (a), Ru/TNSTs-4 (b), and Ru/TNSTs-6 (c) catalysts.

The evaluation of the catalytic performance of the three prepared catalysts was conducted through the selective hydrogenation reaction of benzene, which resulted in the exclusive detection of cyclohexene and cyclohexane as products. In Figure 5A-C, the trends of content variances for cyclohexane, benzene, and cyclohexene with reaction time are exhibited for three nanocomposite catalysts in the selective hydrogenation reaction of benzene. Specifically, the content of benzene exhibits a declining trend throughout the reaction, the cyclohexane content escalates monotonically, and the cyclohexene content presents a parabolic trend. It is evident that the Ru/TNSTs-2 and Ru/TNSTs-4 catalysts exhibit superior catalytic activity. This enhanced performance is ascribed to

Preprints (www.preprints.org) | NOT PEER-REVIEWED | Posted: 12 December 2023 doi:10.20944/preprints202312.0881.v1

their distinctive nanosheet-assembled nanotube architecture, which allows for the ample dispersion of Ru on the nanosheets. The abundance of intersecting nanosheets forestalls the deactivation of Ru microcrystals (deactivation may be due to agglomeration caused by collision between the loaded Ru particles), which ensures the stability of the catalysts, and thus the catalyst continues to function and maintains excellent activity during the reaction process. This is further confirmed by the fact that the catalyst maintains its intact morphology as can be seen from the scanned image of the Ru/TNSTs-4 catalyst after the reaction shown in Figure S5. Further studies showed that the selectivity of cyclohexene decreases with the increase of benzene conversion (Figure 5D), which implied that the content of cyclohexene reached the maximum value at a specific moment 't', in line with the characteristics of the successive reaction. Correspondingly, Figure 5E demonstrates a pronounced linear association between the selectivity for C_6H_{10} and time 't'. The initial selectivity, denoted as S0, was deduced by identifying the intercept on the selectivity-time trajectory. As shown in Table S3, the correlation between annealing time and S_0 shows an interesting "volcano" type trend. This is because the crystalline phase of the catalyst changes as the annealing time increases. The Ru/TNSTs-4 catalyst exhibits a suitable anatase/rutile ratio, where the electron-deficient $Ru^{\delta+}$ formed at the anatase/rutile junction can reduce the adsorption strength of cyclohexene and enhance the rapid desorption of cyclohexene [23,39], leading to a marked enhancement in the catalyst's selectivity. Consequently, an optimal initial selectivity of 95% coupled with a peak cyclohexene yield of 51% was realized for the Ru/TNSTs-4 catalysts, superior to most of the TiO_2-loaded Ru catalysts reported to date (Table S3). This suggests that Ru/TNSTs-4 can be used as an efficient catalyst for the selective hydrogenation of benzene.

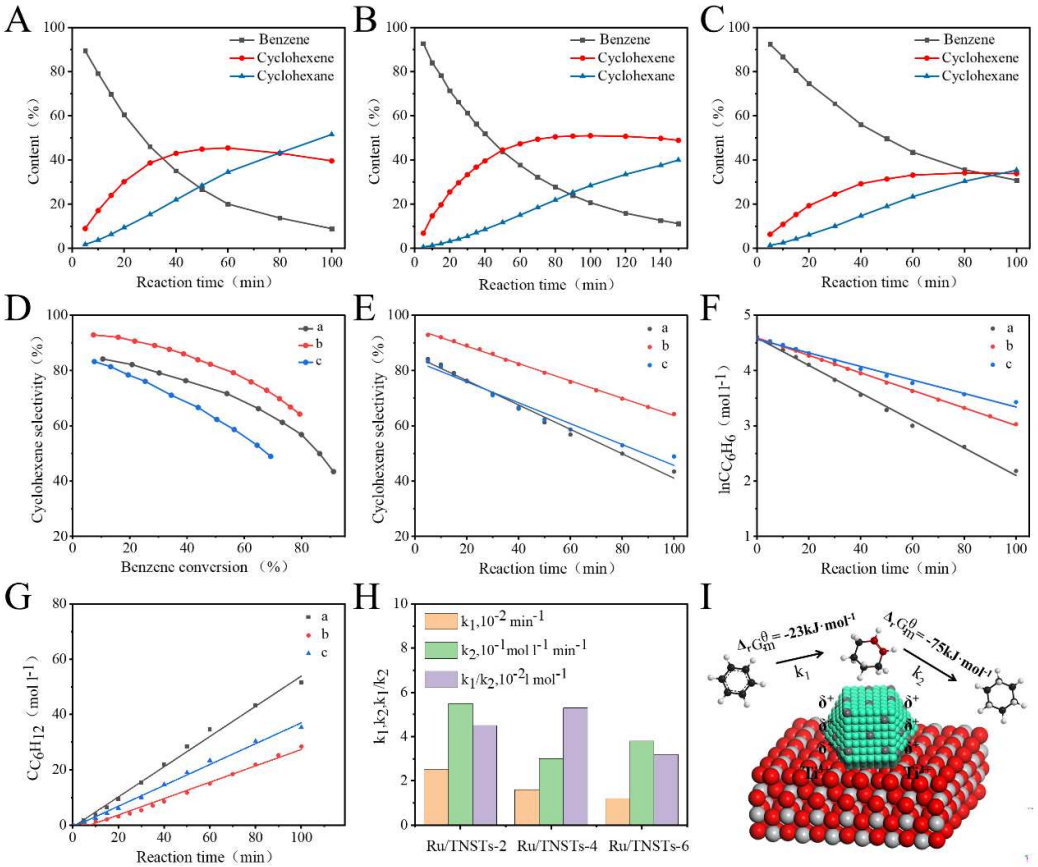

Figure 5. Plots of the process of selective hydrogenation of benzene (A, B, C), cyclohexene selectivity versus benzene conversion (D), cyclohexene selectivity and reaction time (E)，natural logarithm of benzene concentration versus reaction time (F), cyclohexane concentration versus reaction time (G), rate constants for hydrogenation of benzene to cyclohexene (k_1) , hydrogenation of cyclohexene to cyclohexane (k_2), the ratio of k_1: k_2 (H), and cyclohexene selectivity mechanism diagrams (I) of the synthesized Ru/ TNSTs-2 (a), Ru/TNSTs-4 (b), and Ru/TNSTs-6 (c) catalysts.

 doi:10.20944/preprints202312.0881.v1

Evaluation of the catalytic performance of the reaction showed that varying the annealing time improved the selectivity of cyclohexene to a greater extent. Based on the above issues, the kinetic process of the reaction of benzene hydrogenation was further investigated. Generally, the selectivity of cyclohexene, the product of selective benzene hydrogenation, hinges on the relative size of k_1/k_2. When the ratio of k_1/k_2 is larger, the selectivity of cyclohexene tends to be higher. Based on these considerations, in conjunction with the performance data of the catalyst, relationship curves were obtained through kinetic fitting. Figure 5F depicts the correlation between the natural logarithm of benzene concentration and the duration of the reaction, while Figure 5G demonstrates the relationship between the concentration of cyclohexene and reaction time. Both exhibit a significant linear relationship, affirming that the hydrogenation of benzene to cyclohexene aligns with the first-order reaction kinetics under these reaction conditions. Concurrently, the hydrogenation of cyclohexene to cyclohexane obeys zero-order reaction kinetics [40,41]. The origin of selectivity was further probed by determining the rate constants k_1 and k_2 for both steps of benzene hydrogenation as well as cyclohexene hydrogenation. These data were based on the slopes of the above curves. The results show that k_1 tends to decrease with increasing annealing time (Figure 5H). However, k_2 shows a tendency to decrease and then increase, and the k_1/k_2 value reaches its maximum at annealing time of 4 hours. This pattern reflects the trend in cyclohexene selectivity and elucidates the cause of the peak performance of the Ru/TNSTs-4 catalyst in generating cyclohexene yields.

First-principle computations revealed that the activation potential barrier of benzene is 0.8 eV higher than that of cyclohexene [39,42]. This implies that cyclohexene is more susceptible to further deep hydrogenation by hydrogenation reaction on the Ru surface compared to benzene. This further suggests that the selectivity of cyclohexene can be improved if the rapid desorption of cyclohexene can be promoted. Moreover, Ti^{3+} can enhance the inhibition of cyclohexene adsorption and boost the net generation rate of cyclohexene [30]. XPS analysis results corroborate the presence of Ti^{3+} defects on the Ru/TNSTs-4 nanocomposite catalysts (Figure 5I), indicating another potential reason for its heightened selectivity.

3. Experimental section

3.1. Synthesis of TiO_2 nanosheets assembled nanotubes (TNSTs)

Nanotube precursors were prepared using a simple solvothermal and crystallisation process. The preparation of titanium oxide nanotubes was carried out following an enhanced method previously reported [43]. Typically, in a standard procedure, 1 g $TiOSO_4{\cdot}XH_2SO_4{\cdot}yH_2O$ was uniformly dispersed in 20 mL of ethanol, yielding a white solution that was stirred for 2 hours. Subsequently, 10 mL of glycerol and 10 mL of diethyl ether were added to the solution, with stirring being continued for an additional 10 hours. The mixture obtained was then moved into a 100 mL Teflon-coated stainless steel (TSS) autoclave and kept at a temperature of 165℃ for a duration of 8 hours. The product was then centrifuged and washed three times with ethanol to yield a white precipitate. Once dried under vacuum conditions for an entire night, the final specimens were subjected to annealing at a temperature of 600°C for periods of 2, 4, and 6 hours respectively. The resulting TiO_2 nanosheets assembled into nanotubes were labelled as TNSTs-t (t= annealing time).

3.2. Preparation of TNSTs supported Ru catalysts

0.5 g of the synthesized TNSTs was dispersed in 30 mL H_2O. Subsequently, 2.5 mL of aqueous $RuCl_3{\cdot}3H_2O$ (0.2 mol L^{-1}) was added dropwise, and the mixture was stirred for 1 hour. Subsequently, 2.5 mL of an aqueous $NaBH_4$ solution (0.8 mol L^{-1}) was introduced, followed by continuous stirring for one more hour. The resulting precipitate was then washed via centrifugation until chloride ions were completely removed and finally dried under vacuum to yield the Ru/TNSTs-t catalyst.

3.3. Catalytic testing

Performance testing of the liquid-phase benzene selective hydrogenation catalyst was undertaken in a 0.25 L high-temperature and high-pressure reactor from the YZPR series of Yanzheng

 doi:10.20944/preprints202312.0881.v1

Instrument Company. Initially, 0.5 g Ru/TNSTs catalyst, 60 mL H_2O and 12 g $ZnSO_4·7H_2O$ were introduced into the kettle. Among many additives [9,44,45], $ZnSO_4·7H_2O$ was widely recognized as the best additive to enhance the selectivity of cyclohexene effectively [5,46]. Subsequently 30 mL of benzene was added to the storage tank. The reactor and storage tank underwent a purging process with hydrogen for five times, then the temperature was gradually elevated at 5 °C / min. Once the temperature hit 140 °C, the hydrogen pressure was adjusted to 4.0 MPa and the stirring rate was established at 800 revolutions per minute, after which the system was subjected to a pre-treatment phase lasting 4 hours. Subsequently, 30 mL of benzene was introduced from the storage tank, the timer was initiated, and the hydrogen pressure was adjusted to 5.0 MPa. Sample extracts were taken every 5 minutes, and the oil phase was analyzed for cyclohexene, cyclohexane, and benzene content using a gas chromatograph. By applying the area-corrected normalization method, the product concentration was determined, from which the corresponding conversion and cyclohexene selectivity were derived.

3.4. Instrumentation and characterization

The crystalline phase of all samples was determined using a D/Max-2500/PC X-ray diffractometer with Cu Ka radiation (λ=1.5418 Å). The measurements were taken over an angle (2θ) range of 5 to 80° at a scanning rate of 8°/min. N2 adsorption-desorption experiments were conducted on a Micromeritics ASAP 2020 instrument. The specific surface area and pore size distribution were calculated using the Brunauer-Emmett-Teller (BET) and Barrett-Joyner-Halenda (BJH) methods, respectively. The structural details and surface morphology of the samples were explored using a suite of imaging technologies. FESEM (Zeiss SUPRA 55) and HRSEM (SU8200) provided insights into the fine surface features. Internal structures were examined through TEM (Hitachi-7700) and detailed lattice arrangement arrangements via HRTEM (FEI TALOS F200). For advanced characterization, HAADF-STEM and EDS analyses were conducted to delve into the elemental composition and further structural information of the samples. EPR spectra were recorded at room temperature after exposing the sample to UV light for 15 minutes (λ = 355 nm from an Nd: YAG laser), utilizing a Bruker E500 spectrometer for the measurements. To assess the chemical states, XPS analyses were carried out with an ESCALAB MK II system, which features a monochromatic Al-Kα X-ray source. The usual calibration using the adventitious C 1s peak at 284.8 eV was not feasible due to overlap with Ru 3d3/2 signals. Therefore, calibration of binding energy (BE) was instead referenced to the Ti 2p3/2 peak of TiO_2 at a BE of 458.8 eV to ensure accuracy.

4. Conclusions

This work presents the successful development of a ruthenium catalyst anchored on titanium dioxide nanosheet-tubes, which exhibits superior selectivity and efficiency in the hydrogenation of benzene to cyclohexene. Detailed characterization results showed that the phases of TiO_2 carriers could be adjusted with the annealing time, and the optimal catalyst performance was confirmed as 4 hours. By employing this refined Ru/TNSTs-4 catalyst, we achieved a high initial selectivity of 95%. The experimental results demonstrate that the electron deficiency of ruthenium plays an important role in enhancing the selectivity of the catalyst, primarily by promoting the more effective desorption of cyclohexene. Simultaneously, the presence of Ti^{3+} impeded further adsorption of cyclohexene, hence restricted its deep hydrogenation, which in turn maximized selectivity. In addition, the unique morphology of the nanotubes ensured the stability of the catalyst and enhances its activity. Overall, through the effective design of crystalline phase engineering, we conducted a thorough exploration of the effects of valence states of metal-based catalysts and defect-induced alterations in benzene adsorption and cyclohexene desorption. As a result, the catalytic performance was significantly improved, and a promising approach has been developed for the fabrication of efficient metal-support catalysts.

Supplementary Materials: The following supporting information can be downloaded at the website of this paper posted on Preprints.org, Figure S1: SEM images of of TNSTs-2(a,b), TNSTs-4(c,d), and TNSTs-6(e,f); Figure S2: TEM images of Ru/TNSTs-2(a-c) and TNSTs-6(d-f); Figure S3: XRD patterns of TNSTs-2(a), TNSTs-4(b), and TNSTs-6(c); Figure S4: XRD patterns (A) of Ru/TNSTs-2(a), Ru/TNSTs-4(b), and Ru/TNSTs-6(c); Figure S5: SEM images of TNSTs-4 after reaction; Table S1: Structure parameters of various samples; Table S2: The binding energy of Ru 3d5/2 of the catalyst;Table S1: Results of benzene selective hydrogenation over TiO_2 supported Ru catalysts reported in recent literature.

Author Contributions: S.W.: Conceptualization, Methodology, Writing-Original draft preparation. X.C.: Investigation, Data Curation. S.X. and X.Z.: Investigation, Formal analysis. Q.Z.: Investigation, Formal analysis. L.H.: Resources, Writing-Reviewing and Editing. Y.W.: Conceptualization, Writing-Reviewing and Editing. F.G.: Conceptualization, Writing-Reviewing and Editing. All authors have read and agreed to the published version of the manuscript.

Funding: The authors acknowledge the financial support from the Natural Science Foundation of Hebei Province (Grant No. 22281403Z, B2021203016, 236Z4405G) and Hebei Youth Top-notch Talent Support Program. The authors thank the subsidy for Hebei Key Laboratory of Applied Chemistry after Operation Performance (22567616H).

Data Availability Statement: The data presented in this study are available in the article.

Conflicts of Interest: The authors declare no conflict of interest.

References

1. Pu, J.-C.; Doka Dari, M.; Tang, X.-Q.; Yuan, P.-Q. Diffusion of benzene through water film confined in silica mesopores: Effect of competitive adsorption of solvent. *Chemical Engineering Science* **2020**, *224*, doi:10.1016/j.ces.2020.115793.
2. Spod, H.; Lucas, M.; Claus, P. Selective Hydrogenation of Benzene to Cyclohexene over 2Ru/La_2O_3-ZnO Catalyst without Additional Modifiers. *ChemCatChem* **2016**, *8*, 2659-2666, doi:10.1002/cctc.201600493.
3. Melgo, M.S.; Lindner, A.; Schuchardt, U. Wacker oxidation of cyclohexene in the presence of $Pd(NO_3)_2$/$CuSO_4$/$H_3PMo_{12}O_{40}$. *Applied Catalysis A: General* **2004**, *273*, 217-221, doi:10.1016/j.apcata.2004.06.035.
4. Chen, Z.; Sun, H.; Peng, Z.; Gao, J.; Li, B.; Liu, Z.; Liu, S. Selective Hydrogenation of Benzene: Progress of Understanding for the Ru-Based Catalytic System Design. *Industrial & Engineering Chemistry Research* **2019**, *58*, 13794-13803, doi:10.1021/acs.iecr.9b01475.
5. Foppa, L.; Dupont, J. Benzene partial hydrogenation: advances and perspectives. *Chem Soc Rev* **2015**, *44*, 1886-1897, doi:10.1039/c4cs00324a.
6. He, H.; Meyer, R.J.; Rioux, R.M.; Janik, M.J. Catalyst Design for Selective Hydrogenation of Benzene to Cyclohexene through Density Functional Theory and Microkinetic Modeling. *ACS Catalysis* **2021**, *11*, 11831-11842, doi:10.1021/acscatal.1c02630.
7. Nagahara, H.; Ono, M.; Konishi, M.; Fukuoka, Y. Partial hydrogenation of benzene to cyclohexene. *Applied Surface Science* **1997**, *121-122*, 448-451, doi:10.1016/s0169-4332(97)00325-5.
8. Jiang, L.; Zhou, G. Promoting the performances of Ru on hierarchical TiO_2 nanospheres exposed {0 0 1} facets in benzene semi-hydrogenation by manipulating the metal-support interfaces. *Journal of Catalysis* **2020**, *382*, 97-108, doi:10.1016/j.jcat.2019.12.017.
9. Sun, H.; Fan, Y.; Sun, X.; Chen, Z.; Li, H.; Peng, Z.; Liu, Z. Effect of $ZnSO_4$, $MnSO_4$ and $FeSO_4$ on the Partial Hydrogenation of Benzene over Nano Ru-Based Catalysts. *Int J Mol Sci* **2021**, *22*, doi:10.3390/ijms22147756.
10. Peng, Z.; Liu, X.; Lin, H.; Wang, Z.; Li, Z.; Li, B.; Liu, Z.; Liu, S. Surface engineering on a nanocatalyst: basic zinc salt nanoclusters improve catalytic performances of Ru nanoparticles. *Journal of Materials Chemistry A* **2016**, *4*, 17694-17703, doi:10.1039/c6ta08529f.
11. Zhong, Z.; Luo, B.; Lin, C.; Yin, T.; Tian, Z.; Wang, C.; Chen, Y.; Wu, Y.; Shu, R. Ultrafast microfluidic preparation of highly dispersed Ru/TiO_2 catalyst for the hydrodeoxygenation of lignin-derived phenolic compounds. *Fuel* **2023**, *340*, doi:10.1016/j.fuel.2023.127567.
12. Zhang, X.; Luo, L.; Yun, R.; Pu, M.; Zhang, B.; Xiang, X. Increasing the Activity and Selectivity of TiO_2-Supported Au Catalysts for Renewable Hydrogen Generation from Ethanol Photoreforming by Engineering Ti^{3+} Defects. *ACS Sustainable Chemistry & Engineering* **2019**, *7*, 13856-13864, doi:10.1021/acssuschemeng.9b02008.
13. Wang, Y.; Wang, X.; Yan, Z.; Xu, C.; Zhang, W.; Ban, H.; Li, C. Activation reconstructing CuZnO/SiO_2 catalyst for CO_2 hydrogenation. *Journal of Catalysis* **2022**, *412*, 10-20, doi:10.1016/j.jcat.2022.06.003.
14. Wang, S.; Feng, K.; Zhang, D.; Yang, D.; Xiao, M.; Zhang, C.; He, L.; Yan, B.; Ozin, G.A.; Sun, W. Stable Cu Catalysts Supported by Two-dimensional SiO(2) with Strong Metal-Support Interaction. *Adv Sci (Weinh)* **2022**, *9*, e2104972, doi:10.1002/advs.202104972.

15. Diao, Y.; Wang, H.; Chen, B.; Zhang, X.; Shi, C. Modulating morphology and textural properties of Al_2O_3 for supported Ni catalysts toward plasma-assisted dry reforming of methane. *Applied Catalysis B: Environmental* **2023**, *330*, doi:10.1016/j.apcatb.2023.122573.
16. Muravev, V.; Simons, J.F.M.; Parastaev, A.; Verheijen, M.A.; Struijs, J.J.C.; Kosinov, N.; Hensen, E.J.M. Operando Spectroscopy Unveils the Catalytic Role of Different Palladium Oxidation States in CO Oxidation on Pd/CeO(2) Catalysts. *Angew Chem Int Ed Engl* **2022**, *61*, e202200434, doi:10.1002/anie.202200434.
17. Tsiotsias, A.I.; Hafeez, S.; Charisiou, N.D.; Al-Salem, S.M.; Manos, G.; Constantinou, A.; AlKhoori, S.; Sebastian, V.; Hinder, S.J.; Baker, M.A.; et al. Selective catalytic deoxygenation of palm oil to produce green diesel over Ni catalysts supported on ZrO_2 and CeO2–ZrO_2: Experimental and process simulation modelling studies. *Renewable Energy* **2023**, *206*, 582-596, doi:10.1016/j.renene.2023.02.038.
18. Hu, X.; Fan, Q.; Tan, M.; Luo, Y.; Wu, X.; Manuputty, M.Y.; Ding, J.; Choksi, T.S.; Kraft, M.; Xu, R.; et al. Investigating the impact of dynamic structural changes of Au/rutile catalysts on the catalytic activity of CO oxidation. *Carbon Energy* **2023**, doi:10.1002/cey2.412.
19. Wang, K.; He, S.; Lin, Y.; Chen, X.; Dai, W.; Fu, X. Photo-enhanced thermal catalytic CO_2 methanation activity and stability over oxygen-deficient Ru/TiO_2 with exposed TiO_2 {001} facets: Adjusting photogenerated electron behaviors by metal-support interactions. *Chinese Journal of Catalysis* **2022**, *43*, 391-402, doi:10.1016/s1872-2067(21)63825-1.
20. Wang, F.; Kishimoto, H.; Develos-Bagarinao, K.; Yamaji, K.; Horita, T.; Yokokawa, H. Encroachment of titanium oxide on Ni surface for Ni/TiO_2 under reducing atmosphere. *Solid State Ionics* **2016**, *288*, 130-134, doi:10.1016/j.ssi.2016.01.027.
21. Song, Y.; Sun, Z.; Fan, G.; Yang, L.; Li, F. Regulating Surface-Interface Structures of Zn-Incorporated LiAl-LDH Supported Ru Catalysts for Efficient Benzene Hydrogenation to Produce Cyclohexene. *ChemCatChem* **2022**, *14*, doi:10.1002/cctc.202200125.
22. Zhan, Y.; Zhou, C.; Jin, F.; Chen, C.; Jiang, L. Ru/TiO_2 catalyst for selective hydrogenation of benzene: Effect of surface hydroxyl groups and spillover hydrogen. *Applied Surface Science* **2020**, *525*, doi:10.1016/j.apsusc.2020.146627.
23. Zhou, G.; Jiang, L.; He, D. Ru nanoparticles on TiO_2 with various anatase-to-rutile ratios tuned by selective chemical dissolution: Effect of support polymorph composition on selective benzene hydrogenation. *Applied Catalysis A: General* **2019**, *575*, 65-73, doi:10.1016/j.apcata.2019.02.021.
24. Zhou, G.; Dou, R.; Bi, H.; Xie, S.; Pei, Y.; Fan, K.; Qiao, M.; Sun, B.; Zong, B. Ru nanoparticles on rutile/anatase junction of P25 TiO_2 : Controlled deposition and synergy in partial hydrogenation of benzene to cyclohexene. *Journal of Catalysis* **2015**, *332*, 119-126, doi:10.1016/j.jcat.2015.09.016.
25. Jiang, L.; Zhou, G. Distinguishing the roles of TiO_2 {1 0 1}, {0 0 1}, and {0 1 0} facets in benzene semi-hydrogenation over Ru/TiO_2 catalysts. *Applied Surface Science* **2021**, *535*, doi:10.1016/j.apsusc.2020.147709.
26. Shi, R.; Wang, X.; Zhou, G. Electronic metal − support interaction directed electron-deficient nanoparticulate Ru on Ti_3C_2 MXene-derived TiO_2 nanoflowers for robust benzene semi-hydrogenation. *Applied Surface Science* **2023**, *624*, doi:10.1016/j.apsusc.2023.157159.
27. Zhou, G.; Wang, F.; Shi, R. Nanoparticulate Ru on morphology-manipulated and Ti^{3+} defect-riched TiO_2 nanosheets for benzene semi-hydrogenation. *Journal of Catalysis* **2021**, *398*, 148-160, doi:10.1016/j.jcat.2021.04.017.
28. Zhu, F.; Wen, J.; Guo, H.; An, J.; Wang, G.; Ren, G.; Ma, X. Low-temperature catalytic performance improvement of Ru/TiO_2{001} for o-dichlorobenzene oxidation. *Chemical Engineering Journal* **2023**, *473*, doi:10.1016/j.cej.2023.145186.
29. Lin, W.; Chen, Y.; Zhang, Y.; Zhang, Y.; Wang, J.; Wang, L.; Xu, C.C.; Nie, R. Surface Synergetic Effects of Ni–ReOx for Promoting the Mild Hydrogenation of Furfural to Tetrahydrofurfuryl Alcohol. *ACS Catalysis* **2023**, *13*, 11256-11267, doi:10.1021/acscatal.3c01217.
30. Wang, X.; Wang, Z.; Zhou, L.; Liu, Y.; Yang, Y.; Zhang, L.; Shang, Z.; Li, H.; Xiao, T.; Zhang, C.; et al. Efficient hydrodeoxygenation of guaiacol to phenol over Ru/Ti–SiO_2 catalysts: the significance of defect-rich TiOx species. *Green Chemistry* **2022**, *24*, 5822-5834, doi:10.1039/d2gc01714h.
31. Wu, T.; Zhao, H.; Zhu, X.; Xing, Z.; Liu, Q.; Liu, T.; Gao, S.; Lu, S.; Chen, G.; Asiri, A.M.; et al. Identifying the Origin of Ti($^{3+}$) Activity toward Enhanced Electrocatalytic N(2) Reduction over TiO(2) Nanoparticles Modulated by Mixed-Valent Copper. *Adv Mater* **2020**, *32*, e2000299, doi:10.1002/adma.202000299.
32. Hu, J.; Zhang, S.; Cao, Y.; Wang, H.; Yu, H.; Peng, F. Novel Highly Active Anatase/Rutile TiO_2 Photocatalyst with Hydrogenated Heterophase Interface Structures for Photoelectrochemical Water Splitting into Hydrogen. *ACS Sustainable Chemistry & Engineering* **2018**, *6*, 10823-10832, doi:10.1021/acssuschemeng.8b02130.
33. Lan, K.; Wang, R.; Wei, Q.; Wang, Y.; Hong, A.; Feng, P.; Zhao, D. Stable Ti^{3+} Defects in Oriented Mesoporous Titania Frameworks for Efficient Photocatalysis. *Angewandte Chemie International Edition* **2020**, *59*, 17676-17683, doi:10.1002/anie.202007859.

34. Wu, P.; Lyu, S.; Tian, Y.; Zhao, D.; Ye, J.; She, M.; Song, S.; Ding, T.; Li, X. Identification of active sites for preferential oxidation of CO over Ru/TiO_2 catalysts via tuning metal–support interaction. *Chemical Engineering Journal* **2023**, *475*, doi:10.1016/j.cej.2023.146051.
35. Zhao, Z.; Jiang, Q.; Wang, Q.; Wang, M.; Zuo, J.; Chen, H.; Kuang, Q.; Xie, Z. Effect of Rutile Content on the Catalytic Performance of Ru/TiO_2 Catalyst for Low-Temperature CO_2 Methanation. *ACS Sustainable Chemistry & Engineering* **2021**, *9*, 14288-14296, doi:10.1021/acssuschemeng.1c05565.
36. Qiu, J.-Y.; Feng, H.-Z.; Chen, Z.-H.; Ruan, S.-H.; Chen, Y.-P.; Xu, T.-T.; Su, J.-Y.; Ha, E.-N.; Wang, L.-Y. Selective introduction of surface defects in anatase TiO_2 nanosheets for highly efficient photocatalytic hydrogen generation. *Rare Metals* **2022**, *41*, 2074-2083, doi:10.1007/s12598-021-01929-4.
37. Chen, L.-N.; Wang, S.-H.; Zhang, P.-Y.; Chen, Z.-X.; Lin, X.; Yang, H.-J.; Sheng, T.; Lin, W.-F.; Tian, N.; Sun, S.-G.; et al. Ru nanoparticles supported on partially reduced TiO_2 as highly efficient catalyst for hydrogen evolution. *Nano Energy* **2021**, *88*, doi:10.1016/j.nanoen.2021.106211.
38. Tang, M.; Tong, Q.; Li, Y.; Jiang, R.; Shi, L.; Shen, F.; Wei, Y.; Liu, Z.; Liu, S.; Zhang, J.; et al. Effective and selective electrocatalytic nitrate reduction to ammonia on urchin-like and defect-enriched titanium oxide microparticles. *Chinese Chemical Letters* **2023**, *34*, doi:10.1016/j.cclet.2023.108410.
39. Zhou, G.; Dong, Y.; He, D. Bimetallic Ru–M/TiO_2 (M = Fe, Ni, Cu, Co) nanocomposite catalysts facribated by galvanic replacement: Structural elucidation and catalytic behavior in benzene selective hydrogenation. *Applied Surface Science* **2018**, *456*, 1004-1013, doi:10.1016/j.apsusc.2018.06.206.
40. Hao, F.; Zheng, J.; Ouyang, D.; Xiong, W.; Liu, P.; Luo, H. Selective hydrogenation of benzene over Ru supported on surface modified TiO_2. *Korean Journal of Chemical Engineering* **2021**, *38*, 736-746, doi:10.1007/s11814-020-0689-9.
41. Liu, S.C.; Guo, Y.Q.; Yang, X.L.; Ji, Y.L.; Luo, G. Kinetic Equations for Liquid-Phase Selective Hydrogenation of Benzene to Cyclohexene. *Chinese Journal of Catalysis* **2003**, *24*, 42-46.
42. Fan, C.; Zhu, Y.-A.; Zhou, X.-G.; Liu, Z.-P. Catalytic hydrogenation of benzene to cyclohexene on Ru(0001) from density functional theory investigations☆. *Catalysis Today* **2011**, *160*, 234-241, doi:10.1016/j.cattod.2010.03.075.
43. Zhang, X.; Hu, W.; Zhang, K.; Wang, J.; Sun, B.; Li, H.; Qiao, P.; Wang, L.; Zhou, W. Ti^{3+} Self-Doped Black TiO_2 Nanotubes with Mesoporous Nanosheet Architecture as Efficient Solar-Driven Hydrogen Evolution Photocatalysts. *ACS Sustainable Chemistry & Engineering* **2017**, *5*, 6894-6901, doi:10.1021/acssuschemeng.7b01114.
44. Zhang, P.; Wu, T.; Jiang, T.; Wang, W.; Liu, H.; Fan, H.; Zhang, Z.; Han, B. Ru–Zn supported on hydroxyapatite as an effective catalyst for partial hydrogenation of benzene. *Green Chem.* **2013**, *15*, 152-159, doi:10.1039/c2gc36596k.
45. Fan, G.-Y.; Jiang, W.-D.; Wang, J.-B.; Li, R.-X.; Chen, H.; Li, X.-J. Selective hydrogenation of benzene to cyclohexene over RuCoB/γ-Al_2O_3 without additive. *Catalysis Communications* **2008**, *10*, 98-102, doi:10.1016/j.catcom.2008.08.002.
46. Yu, X.-L.; Li, Y.; Xin, S.-M.; Yuan, P.-Q.; Yuan, W.-K. Partial Hydrogenation of Benzene to Cyclohexene on Ru@XO_2 (X = Ti, Zr, or Si). *Industrial & Engineering Chemistry Research* **2018**, *57*, 1961-1967, doi:10.1021/acs.iecr.7b04642.